

Wasserstein Distances for Stereo Disparity Estimation

Divyansh Garg¹ Yan Wang¹ Bharath Hariharan¹

Mark Campbell¹ Kilian Q. Weinberger¹ Wei-Lun Chao²

¹Cornell University, Ithaca, NY ²The Ohio State University, Columbus, OH
 {dg595, yw763, bh497, mc288, kqw4}@cornell.edu chao.209@osu.edu

Abstract

Existing approaches to depth or disparity estimation output a distribution over a set of pre-defined discrete values. This leads to inaccurate results when the true depth or disparity does not match any of these values. The fact that this distribution is usually learned indirectly through a regression loss causes further problems in ambiguous regions around object boundaries. We address these issues using a new neural network architecture that is capable of outputting arbitrary depth values, and a new loss function that is derived from the Wasserstein distance between the true and the predicted distributions. We validate our approach on a variety of tasks, including stereo disparity and depth estimation, and the downstream 3D object detection. Our approach drastically reduces the error in ambiguous regions, especially around object boundaries that greatly affect the localization of objects in 3D, achieving the state-of-the-art in 3D object detection for autonomous driving.

1 Introduction

Depth estimation from stereo images is a long standing task in computer vision [28, 34]. It is a key component of many downstream problems, ranging from 3D object detection in autonomous vehicles [9, 20, 31, 39, 49] to graphics applications such as novel view generation [22, 50]. The importance of this task in practical applications has led to a flurry of recent research. Convolutional networks have now superseded more classical techniques, and led to significant improvements in accuracy [5, 25, 40, 53].

These techniques estimate depth by finding accurate pixel correspondences and estimating the *disparity* between their *X*-coordinates, which is inversely proportional to depth. Because pixels have integral coordinates, so does the estimated disparity — causing even the resulting depth estimates to be discrete. This introduces inaccuracy, as the ground-truth disparity and depth are naturally real-valued. This discrepancy is typically addressed by predicting a *categorical distribution* over a fixed set of discrete values, and then computing the *expected* depth from this distribution, which can in theory be any arbitrary real value (within the range of the set) [5, 13, 40, 49, 53].

In this paper, we argue that such a design choice may lead to inaccurate depth estimates, especially around object boundaries. For example, in Figure 1 we show the pixels (back-projected into 3D

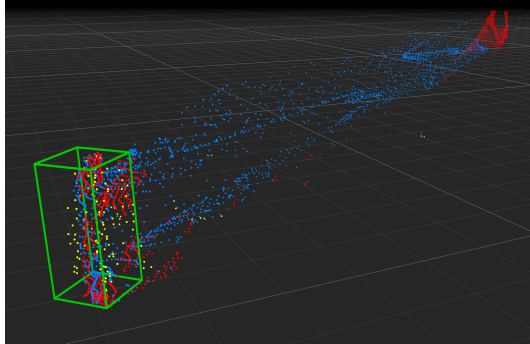


Figure 1: **The effect of our continuous disparity network (CDN).** We show a person (green box) in front of a wall. The blue 3D points are obtained using PSMNet [5]. The red points from our **CDN** model are much better aligned with the shape of the objects: they do not suffer the streaking artifacts near edges. Yellow points are from the ground-truth LiDAR. (One floor square is 1mx1m.)

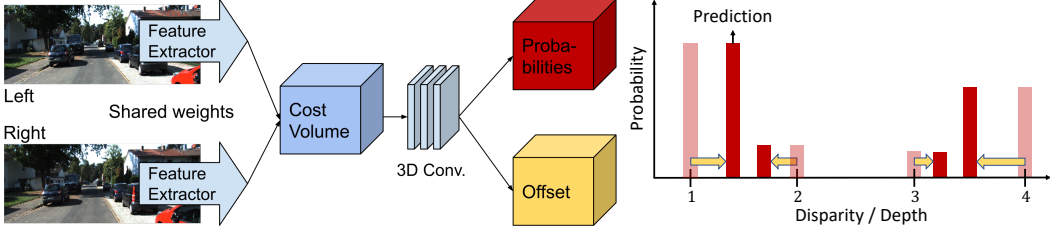


Figure 2: **Continuous disparity network (CDN)**. We propose to predict a *real-value* offset (yellow arrows) for each pre-defined discrete disparity value (e.g., $\{1, 2, 3, 4\}$), turning a categorical distribution (magenta bars) to a continuous distribution (red bars), from which we can output the mode disparity for accurate estimation.

using the depth estimates) along the boundary between a person in the foreground at 30m depth and a wall in the background at 70m depth. The predicted depth distribution of these border pixels is likely to be multi-modal, having two peaks around 30 and 70 meters. Simply taking the mean outputs a low probability value in between the two modes (e.g., 50m). Such “smoothed” depth estimates can have a strong negative impact on subsequent 3D object detection, as they “smear” the pedestrian around its edges towards the background (note the many blue points between the wall and the pedestrian). A bounding box including all these trailing points, far from the actual person, would strongly misrepresent the scene’s geometry. What may further aggravate the problem is how the distribution is usually learned. Existing approaches mostly learn the distribution via a regression loss: minimizing the distance between the mean value and the ground truth [13, 49]. In other words, there is no direct supervision to teach the model to assign higher probabilities around the truth depth.

To address these issues, we propose a novel neural network architecture for stereo disparity estimation that is capable of outputting a distribution over *arbitrary* disparity values, from which we can directly take the mode and bypass the mean. As with existing work, our model predicts a probability for each disparity value in a pre-defined, discrete set. Additionally, it predicts a real-valued *offset* for each discrete value. This is a simple architectural modification, but it has a profound impact. With these offsets, the output is converted from a discrete categorical distribution to a *continuous* distribution over disparity values: a mixture of Dirac delta functions, centered at the pre-defined discrete values shifted by predicted offsets¹. This simple addition of predicted offsets allows us to use the mode as the prediction during inference, instead of the mean, guaranteeing that the predicted depth has a high estimated probability. Figure 2 illustrates our model, **continuous disparity network (CDN)**.

Next, we propose a novel loss function that provides a more informative objective during training. Concretely, we allow uni- or multi-modal ground truth depth distributions (obtained from nearby pixels) and represent them as (mixtures of) Dirac delta functions. The learning objective is then to minimize the divergence between the predicted and the ground truth distributions. Noting that the two distributions might not have a common support, we apply the Wasserstein distance [38] to measure the divergence. While computing the exact Wasserstein distance of arbitrary distributions can be time consuming, computing it for one-dimensional distributions (e.g., distributions of one-dimensional disparity) enjoys efficient solutions, creating negligible training overhead.

Our proposed approach is both mathematically well founded and practically extremely simple. It is compatible with most existing stereo depth or disparity estimation approaches — we only need to add an additional offset branch and replace the commonly used regression loss by the Wasserstein distance. We validate our approach using multiple existing stereo networks [5, 49, 53] on three tasks: stereo disparity estimation [25], stereo depth estimation [10], and 3D object detection [10]. The last is a downstream task using stereo depth as the input to detect objects in 3D. We conduct comprehensive experiments and show that our algorithm lead to significant improvement in all three tasks.

2 Background

Stereo techniques rely on two cameras oriented parallel and translated horizontally relative to each other [44]. In this setting, for a pixel (u, v) in one image, the corresponding pixel in the second

¹Our work is reminiscent of G-RMI pose estimator [28], which predicts the heatmaps (at fixed locations) and offsets for each keypoint. Our work is also related to one-stage object detectors [21, 23, 33] that predict the class probabilities and box offsets for each anchor box.

image is constrained to be at $(u + D(u, v), v)$, where $D(u, v)$ is called the *disparity* of the pixel. The disparity is inversely proportional to the *depth* $Z(u, v)$: $D(u, v) = \frac{f \times b}{Z(u, v)}$, where b is the translation between the cameras (called the *baseline*) and f is the focal length of the cameras. Stereo depth estimation techniques typically first estimate disparity in units of pixels and then exploit the reciprocal relationship to approximate depth. The basic approach is to compare pixels (u, v) in the left image I_l with pixels $(u, v + d)$ in the right image I_r for different values of d , and find the best match. Since pixel coordinates are constrained to be integers, d is constrained to be an integer as well. The estimated disparity is thus an integer, forcing the estimated depth to be one of a few discrete values.

Instead of producing a single integer-valued disparity value, modern pipelines produce a *distribution* over these possible disparities. They do this by constructing a 4D *disparity feature volume*, C_{disp} , in which $C_{\text{disp}}(u, v, d, :)$ is a feature vector that captures the difference in appearance between $I_l(u, v)$ and $I_r(u, v + d)$. This feature vector can be, for instance, the concatenation of the feature vectors of the two pixels, in turn obtained by running a convolutional network on each image. The disparity feature volume is then passed through a series of 3D convolutional layers, culminating in a cost for each disparity value d for each pixel, $S_{\text{disp}}(u, v, d)$ [5]. By taking softmax along the disparity dimension, one can turn $S_{\text{disp}}(u, v, d)$ into a probability distribution. Because we only consider integral disparity values, this distribution is a categorical distribution over the possible disparity values (e.g., $d \in \{0, \dots, 191\}$). One can then obtain the disparity $D(u, v)$, for example, by $\text{argmax}_d \text{softmax}(-S_{\text{disp}}(u, v, d))$. However, in order to obtain continuous disparity estimates beyond integer-valued disparities, [5, 13, 40, 53] apply the following weighted combination (i.e., mean),

$$D(u, v) = \sum_d \text{softmax}(-S_{\text{disp}}(u, v, d)) \times d. \quad (1)$$

The whole neural network can be learned end-to-end, including the image feature extractor and 3D convolution kernels, to minimize the disparity error (on one image)

$$\sum_{(u, v) \in \mathcal{A}} \ell(D(u, v) - D^*(u, v)), \quad (2)$$

where ℓ is the smooth L1 loss, D^* is the ground truth map, and \mathcal{A} contains pixels with ground truths.

Recently, [49] argue that learning with Equation 2 may over-emphasize nearby depths, and accordingly propose to learn the network directly to minimize the depth loss. Specifically, they constructed depth cost volume $S_{\text{depth}}(u, v, z)$, rather than $S_{\text{disp}}(u, v, d)$, and predicted the continuous depth by

$$Z(u, v) = \sum_z \text{softmax}(-S_{\text{depth}}(u, v, z)) \times z. \quad (3)$$

The entire network is learned to minimize the distance to the ground truth depth map Z

$$\sum_{(u, v) \in \mathcal{A}} \ell(Z(u, v) - Z^*(u, v)). \quad (4)$$

In this paper, we argue that the design choices to output continuous values (Equation 1 and Equation 3) can be harmful to pixels in ambiguous regions, and the objective functions for learning the networks (Equation 2 and Equation 4) do not directly match the predicted distribution to the true one. The most similar work to ours is [54], which learns the network with a distribution matching loss on $\text{softmax}(-S_{\text{disp}}(u, v, d))$; however, they still need to apply Equation 1 to obtain continuous estimates.

Stereo-based 3D object detection. 3D object detection has attracted significant attention recently, especially for the application of self-driving cars [1, 4, 6, 10, 11, 14]. While many algorithms rely on the expensive LiDAR sensor as input [16, 17, 30, 35, 45], several recent papers have shown promising accuracy using the much cheaper stereo images [9, 15, 18, 20, 29, 42, 51]. One particular framework is Pseudo-LiDAR [31, 39, 49], which converts stereo depth estimates into a 3D point cloud that can be inputted to any existing LiDAR-based detector, achieving the state-of-the-art results.

3 Disparity Estimation

For brevity, in the following we mainly discuss disparity estimation. The same technique can easily be applied to depth estimation, which are usually adapted from their disparity estimation counterparts.

As reviewed in [section 2](#), many existing stereo networks output a distribution of disparities at each pixel. This distribution is a categorical distribution over discrete disparity values: discrete because they are estimated as the difference in X -coordinates of corresponding pixels, and as such are integers. Stereo techniques then compute the mean of the distribution to obtain a continuous estimate that is not limited to integral values.

We point out two disadvantages of taking the mean estimate. First, the mean value can deviate from the mode and may wrongly predict values of low probability when the predicted distribution is multi-modal (see [Figure 3](#)). Such multi-modal distributions appear frequently at pixels around the object boundaries. While they collectively occupy only a tiny portion of image pixels, recent studies have shown their particular importance in the downstream tasks like 3D object detection [[19](#), [20](#), [31](#)]. For instance, let us consider a street scene where a car 30m away (a disparity of, say, 10 pixels) is driving on the road towards the camera, with sky as the background. The pixels on the car boundary can either take a disparity of around 10 pixels (for the car) or a disparity of 0 pixels (for the sky). Simply taking the mean likely produces arbitrary disparity estimates between these values, producing depth estimates that are neither on the car nor on the background. The downstream 3D object detector can, therefore, wrongly predict the car orientation and size, potentially leading to accidents. Second, the physical meaning of the mean value is by no means aligned with the true disparity: uncertainty in correspondence might yield a 40% chance of a disparity of 10 pixels and a 60% chance for a disparity of 20 pixels, but this does not mean that the disparity should be 16 pixels.

Instead, a more straightforward way to simultaneously model the uncertainty and output continuous disparity estimates is to extend the support of the output distribution beyond integers.

3.1 Continuous disparity network (CDN)

To this end, we propose a new neural network architecture and output representation for disparity estimation. The output of our network will still be a set of discrete values with corresponding probabilities, but the discrete values *will not be restricted to integers*. The key idea is to start with integral disparity values, and predict *offsets* in addition to probabilities.

Denote by \mathcal{D} the set of integral disparity values. As above, disparity estimation techniques produce a cost $S_{\text{disp}}(u, v, d)$ for every $d \in \mathcal{D}$. A softmax converts this cost into a probability distribution:

$$p(d|u, v) = \begin{cases} \text{softmax}(-S_{\text{disp}}(u, v, d)) & \text{if } d \in \mathcal{D}, \\ 0 & \text{otherwise.} \end{cases} \quad (5)$$

We propose to add a sub-network $b(u, v, d)$ that predicts an offset value for each integral disparity value $d \in \mathcal{D}$. We use this to displace the probability mass at $d \in \mathcal{D}$ to $d' = d + b(u, v, d)$. This results in the following probability distribution:

$$\tilde{p}(d'|u, v) = \begin{cases} \text{softmax}(-S_{\text{disp}}(u, v, d)) & \text{when } d' = d + b(u, v, d), d \in \mathcal{D}, \\ 0 & \text{otherwise.} \end{cases} \quad (6)$$

This can be written as a mixture of Dirac delta functions over arbitrary disparity values d'

$$\tilde{p}(d'|u, v) = \sum_{d \in \mathcal{D}} p(d|u, v) \delta(d' - (d + b(u, v, d))). \quad (7)$$

In other words, \tilde{p} has $|\mathcal{D}|$ supports, each located at $d + b(u, v, d)$ with a weight $p(d|u, v)$. The resulting continuous disparity estimate $D(u, v)$ at (u, v) is the **mode** of $\tilde{p}(d'|u, v)$.

Our network design with a sub-network for offset prediction is reminiscent of G-RMI pose estimator [28] and one-stage 2D object detectors [21, 23, 33]. The former predicts the heatmaps (at fixed locations) and offsets for each keypoint; the latter parameterizes the predicted bounding box coordinates by the anchor box location plus the predicted offset. One may also interpret our approach as a coarse-to-fine depth prediction, first picking the bin centered around $\text{argmax}_{d \in \mathcal{D}} p(d|u, v)$ and then locally adjusting it by an offset.

In our implementation, the sub-network $b(u, v, d)$ shares its feature and computation with $S_{\text{disp}}(u, v, d)$ except for the last block of fully-connected or convolutional layers.

3.2 Learning with Wasserstein distances

We propose to train our disparity network such that the mixture of Dirac delta functions (Equation 7) is directly learned to match the ground truth distribution. Concretely, we represent the distribution of ground truth disparity at a pixel (u, v) , $p^*(d'|u, v)$, as a Dirac delta function centered at the ground truth disparity $d^* = D^*(u, v)$: $p^*(d'|u, v) = \delta(d' - d^*)$. We then employ a learning objective to minimize the divergence (distance) between $\tilde{p}(d'|u, v)$ and $p^*(d'|u, v)$. There are many popular divergence measures between distributions, such as Kullback-Leibler divergence, Jensen-Shannon divergence, total Variation, the Wasserstein distance, etc. In this paper, we choose the Wasserstein distance for one particular reason: $\tilde{p}(d'|u, v)$ and $p^*(d'|u, v)$ may not have any common supports.

The Wasserstein- p distance between two distributions μ, ν over a metric space (X, d) is defined as

$$W_p(\mu, \nu) = \left(\inf_{\gamma \in \Gamma(\mu, \nu)} \mathbb{E}_\gamma d(x, y)^p \right)^{1/p}, \quad (8)$$

where $\Gamma(\mu, \nu)$ denotes the set of all the joint distributions $\gamma(x, y)$ whose marginal distributions $\gamma(x)$ and $\gamma(y)$ are exactly μ and ν , respectively. Intuitively, $\gamma(x, y)$ indicates how much “mass” to be transported from x to y in order to transform the distribution μ to ν .

Estimating the Wasserstein distance is usually non-trivial and requires solving a linear programming problem. One particular exception is when μ and ν are both distributions of one-dimensional variables, which is the case for our distribution over disparity values². Specifically, when ν is a Dirac delta function whose support is located at y^* , the Wasserstein- p distance can be simplified as

$$W_p(\mu, \nu) = (\mathbb{E}_\mu \mathbb{E}_\nu \|x - y\|^p)^{1/p} = (\mathbb{E}_\mu \|x - y^*\|^p)^{1/p}. \quad (9)$$

By plugging $\tilde{p}(d'|u, v)$ and $p^*(d'|u, v)$ into μ and ν respectively, we obtain

$$\begin{aligned} W_p(\tilde{p}, p^*) &= (\mathbb{E}_{\tilde{p}} \|d' - d^*\|^p)^{1/p} = \left(\sum_{d \in \mathcal{D}} p(d|u, v) \|d + b(u, v, d) - d^*\|^p \right)^{1/p} \\ &= \left(\sum_{d \in \mathcal{D}} \text{softmax}(-S_{\text{disp}}(u, v, d)) \|d + b(u, v, d) - d^*\|^p \right)^{1/p}, \end{aligned} \quad (10)$$

based on which we can learn the conventional disparity network (red) and the additional offset sub-network (blue) jointly (i.e., by minimizing Equation 10). We focus on W_1 and W_2 distances.

3.3 Extension: learning with multi-modal ground-truth

One particular advantage of learning to match the distributions is the capability of allowing multiple ground truth values (i.e., a multi-modal ground truth distribution) at a single pixel location. Denote \mathcal{D}^* as the set of ground truth disparity values at a pixel (u, v) , the ground truth distribution becomes

$$p^*(d'|u, v) = \sum_{d^* \in \mathcal{D}^*} \frac{1}{|\mathcal{D}^*|} \delta(d' - d^*). \quad (11)$$

Since $p^*(d'|u, v)$ is not a Dirac delta function, we can no longer apply Equation 9 but the following equation for comparing two one-dimensional distributions [27, 32, 41]

$$W_p(\tilde{p}, p^*) = \left(\int_0^1 \left| \tilde{P}^{-1}(x) - P^{*-1}(x) \right|^p dx \right)^{1/p}, \quad (12)$$

²For dealing with disparity or depth values, our metric space naturally becomes \mathcal{R}^1 .

where \tilde{P} and P^* are the cumulative distribution functions (CDFs) of \tilde{p} and p^* , respectively. For the case $p = 1$, we can rewrite [Equation 12](#) as [37]

$$W_1(\tilde{p}, p^*) = \int_{\mathbb{R}} \left| \tilde{P}(d') - P^*(d') \right| dd'. \quad (13)$$

We note that, both [Equation 12](#) and [Equation 13](#) can be computed efficiently.

While existing datasets do not provide multi-modal ground truths directly, we investigate the following procedure to construct them. For each pixel, we consider a $k \times k$ neighborhood and create a multi-modal distribution by setting the center-pixel disparity with a weight α and the remaining ones each with $\frac{1-\alpha}{k \times k - 1}$. We set $k = 3$ and $\alpha = 0.8$ in the experiment. Our empirical study shows that using a multi-modal ground truth leads to a much faster model convergence.

3.4 Comparisons to related work

Compared to G-RMI pose estimator and one-stage 2D object detectors mentioned in [subsection 3.1](#), our work learns the two (sub-)networks jointly using a single objective function rather than a combination of two separated ones. See [subsection A.3](#) and [subsection B.1](#) in the supplementary material for more comparisons. Liu et al. [24] propose to use the Wasserstein loss for pose estimation to characterize the inter-class correlations; however, they do not predict offsets for pre-defined discrete pose labels. Our work is also related to [3], in which the authors propose to learn the value distribution, instead of the expected value, using the Wasserstein loss for reinforcement learning.

4 Experiments

4.1 Datasets and metrics

Datasets. We evaluate our method on two challenging stereo benchmark datasets, i.e., Scene Flow [25] and KITTI 2015 [26], and on a 3D object detection benchmark KITTI 3D [10, 11].

1) Scene Flow [25]. Scene Flow is a large synthetic dataset containing 35,454 training image pairs and 4,370 testing image pairs, where the ground truth disparity maps are densely provided, which is large enough for directly training deep neural networks.

2) KITTI 2015 [26]. KITTI 2015 is a real-world dataset with street scenes captured from a driving car. KITTI 2015 contains 200 training stereo image pairs with sparse ground truth disparities obtained using LiDAR, and 200 testing image pairs with ground truth disparities held by evaluation server for submission evaluation only. Its small size makes it a challenging dataset.

3) KITTI 3D [10, 11]. KITTI 3D contains 7,481 (pairs of) images for training and 7,518 (pairs of) images for testing. We follow the same training and validation splits as suggested by Chen et al. [7], containing 3,712 and 3,769 images, respectively. For each image, KITTI provides the corresponding Velodyne LiDAR point cloud (for sparse depth ground truths), camera calibration matrices, and 3D bounding box annotations. We evaluate our approach by plugging it into existing stereo-based 3D object detectors [9, 39, 49], which all require stereo depth estimation as a key component.

Metrics. For **1) stereo disparity**, we use two standard metrics: End-Point-Error (EPE), i.e., the average difference of the predicted disparities and their true ones, and k -Pixel Threshold Error (PE), i.e., the percentage of pixels for which the predicted disparity is off the ground-truth by more than k pixels. We use the 1-pixel and 3-pixel threshold errors, denoted as 1PE and 3PE. PE is robust to outliers with large disparity errors, while EPE measures errors to sub-pixel level.

2) stereo depth. We use the Root Mean Square Error (RMSE) $\sqrt{\frac{1}{|\mathcal{A}|} \sum_{(u,v) \in \mathcal{A}} \|z(u,v) - z^*(u,v)\|^2}$ and Absolute Relative Error (ABSR) $\frac{1}{|\mathcal{A}|} \sum_{(u,v) \in \mathcal{A}} \frac{|z(u,v) - z^*(u,v)|}{z^*(u,v)}$, where \mathcal{A} denotes all the pixels having ground truths, and z and z^* are estimated depth and ground truth depth respectively.

3) 3D object detection. We focus on 3D and bird’s-eye-view (BEV) localization and report the results on the official leaderboard and the validation set. Specifically, we focus on the “car” category, following [8, 43]. We report the average precision (AP) at IoU thresholds 0.5 and 0.7. We denote AP for the 3D and BEV tasks by AP_{3D} and AP_{BEV} , respectively. The benchmark defines for each category three cases — easy, moderate, and hard — according to the bounding box height and occlusion and truncation. In general, the easy case corresponds to cars within 30 meters of the ego-car distance.

Table 1: **Disparity results.** We report results on Scene Flow and KITTI 2015 Benchmarks. For Scene Flow, end point errors (EPE) and the 1-pixel and 3-pixel threshold error rates (1PE, 3PE) are reported. For KITTI 2015 we report the standard metrics (using 3PE) for both Non-occluded and All pixels regions. Methods based on **CDN** are highlighted in **blue**. Lower is better. The best result per column in in bold. Best viewed in color.

Method	Scene Flow			KITTI 2015			
	EPE	1PE	3PE	Non Occlusion 3PE		All Areas 3PE	
				Foreground	All	Foreground	All
MC-CNN [52]	3.79	-	-	7.64	3.33	8.88	3.89
GC-Net [13]	2.51	16.9	9.34	5.58	2.61	6.16	2.87
PSMNet [5]	1.09	12.1	4.56	4.31	2.14	4.62	2.32
SegStereo [47]	1.45	-	-	3.70	2.08	4.07	2.25
GwcNet-g [12]	0.77	8.0	3.30	3.49	1.92	3.93	2.11
HD ³ -Stereo [48]	1.08	-	-	3.43	1.87	3.63	2.02
GANet [53]	0.84	9.9	-	3.37	1.73	3.82	1.93
AcfNet [54]	0.87	-	4.31	3.49	1.72	3.80	1.89
Stereo Expansion [46]	-	-	-	3.11	1.63	3.46	1.81
GANet Deep [53]	0.78	8.7	-	3.11	1.63	3.46	1.81
CDN-PSMNet	0.98	9.1	3.99	4.01	2.12	4.34	2.29
CDN-GANet Deep	0.70	7.7	2.98	2.79	1.72	3.20	1.92

4.2 Implementation details

We mainly use the Wasserstein-1 distance (i.e., W_1 loss) for training our **CDN** model. We compare W_1 and \tilde{W}_2^2 losses in the supplementary material.

Stereo disparity. We apply our **continuous disparity network (CDN)** architecture to PSMNet [5] and GANet [53], namely **CDN-PSMNET** and **CDN-GANET**. To keep a fair comparison, we train the models with their default settings. For Scene Flow, the models are trained from scratch with a constant learning rate of 0.001 for 10 epochs. For KITTI 2015, the models pre-trained on Scene Flow are fine-tuned following the default strategy of the vanilla models. We consider disparities in the range of [0, 191] for both datasets. We use a uniform grid of bin size 2 pixels to create the categorical distribution (cf. [Equation 5](#)). We show the effect of bin sizes in the supplementary material.

Stereo depth. We apply **CDN** to the SDN architecture [49], namely **CDN-SDN**. We follow the training procedure in [49]. We consider depths in the range of [0, 80]. We use a uniform grid of bin size 1m to create the categorical distribution.

Stereo 3D object detection. We apply **CDN-SDN** to PSEUDO-LiDAR ++ [49], which uses SDN to estimate depth. We fine-tune the **CDN-SDN** model pre-trained on Scene Flow on KITTI 3D dataset, followed by using an 3D object detector, here P-RCNN [35], to detect 3D bounding boxes of cars. We also apply **CDN** to DSGN [9], the state-of-the-art stereo-based 3D object detector. DSGN uses as a backbone depth estimator based on PSMNET and we replace it with our **CDN** version.

Multi-modal ground-truth. As mentioned in [section 3](#), we create multi-modal ground-truths for a pixel by considering a patch in its $k \times k$ neighborhood. We give the center-pixel disparity a weight $\alpha = 0.8$, and remaining ones an equal weights such that the total sums to 1. In this case, we use [Equation 13](#) as the loss function. We implement a differentiable loss module in Pytorch that can be applied to a batch of image tensors. Please see the supplementary material for details.

Offset range. We predict a single offset $[0, s]$ for each grid value, where s is the bin size.

4.3 Experimental results

Disparity estimation. [Table 1](#) summarizes the main results on disparity estimation. **CDN-GANET** Deep³ achieves the lowest error at all three metrics on Scene Flow. It reduces the error for GANet Deep by 1.0 1PE and 0.08 EPE, both are significant. We see a similar gain on PSMNET as well: **CDN-PSMNET** reduces EPE by 0.09, demonstrating the general applicability of our approach to existing networks.

On KITTI 2015, **CDN-GANET** Deep obtains the lowest error on the *foreground* pixels and performs comparably to other methods on all the pixels. We see a similar gain by **CDN-PSMNET** over PSMNET on the foreground, which is quite surprising, as we do not specifically *re-weight* the loss

³We apply the GANet Deep model introduced in the released code of [53], available at <https://github.com/feihuzhang/GANet>.

Table 2: **3D object detection results on KITTI leaderboard.** We report AP_{BEV} and AP_{3D} (in %) of the **car** category at $IoU = 0.7$ on KITTI test set. The best result of each column is in bold font.

Method	BEV Detection AP			3D Detection AP		
	Easy	Moderate	Hard	Easy	Moderate	Hard
S-RCNN [20]	61.9	41.3	33.4	47.6	30.2	23.7
OC-STEREO [29]	68.9	51.5	43.0	55.2	37.6	30.3
DISP R-CNN [36]	74.1	52.4	43.8	59.6	39.4	32.0
PSEUDO-LiDAR	67.3	45.0	38.4	54.5	34.1	28.3
PSEUDO-LiDAR ++	78.3	58.0	51.3	61.1	42.4	37.0
PSEUDO-LiDAR E2E	79.6	58.8	52.1	64.8	43.9	38.1
CDN-PSEUDO-LiDAR ++	81.3	61.0	52.8	64.3	44.9	38.1
DSGN	82.9	65.0	56.6	73.5	52.2	45.1
CDN-DSGN	83.3	66.2	57.7	74.5	54.2	46.4

Table 3: **Disparity multi-modal results.** We report the EPE, 1PE and 3PE on Scene Flow. The best result of each column is in bold font.

Method	EPE	1PE	3PE
PSMNET	1.09	12.1	4.56
CDN-PSMNET	0.98	9.1	3.99
CDN-PSMNET MM	0.96	9.0	3.96

Table 4: **Depth multi-modal results.** We report the RMSE and ABSR errors on Scene Flow. The best result of each column is in bold font.

Method	RMSE (m)	ABSR
SDN	2.05	0.039
CDN-SDN	1.81	0.030
CDN-SDN MM	1.80	0.028

function towards foregrounds. We thus argue that, most of the pixels whose disparity is ambiguous and hard to estimate correctly (e.g., due to multi-modal distributions) are on the foreground. Indeed, by comparing the error on all pixels and on foreground pixels, we see a much higher value on the foreground. As will be seen in 3D object detection, the large improvement by **CDN** on foreground translates to a higher accuracy on localizing objects.

3D object detection. Table 2 summarizes the results on KITTI 3D test set. Our **CDN** consistently improves the two mainstream approaches, namely, DSGN and PSEUDO-LiDAR. For PSEUDO-LiDAR, we achieve a 2.5%/3.0% gain on AP_{3D}/AP_{BEV} Moderate (the standard metric on the leaderboard) against PSEUDO-LiDAR ++: the only difference is that we replace SDN by our **CDN-SDN** to have better depth estimates. Our approach even outperforms PSEUDO-LiDAR E2E, which fine-tunes the depth network specifically for object detection. We argue that our approach, which can *automatically* focus on the foregrounds, may have a similar effect as end-to-end training with object detection losses. For DSGN, plugging our **CDN-SDN** leads to a notable 2% gain at AP_{3D} , attaining the highest entry of stereo-based 3D detection accuracy on the KITTI leader board.

Multi-modal (MM) ground-truth. We investigate creating the multi-modal (MM) ground-truths for training our models. Table 3 and Table 4 summarize the results on Scene Flow for disparity and depth estimation, respectively. MM training slightly reduces the errors. To better understand how MM ground truths affect network training, we plot the test accuracy along the training epochs in Figure 4: **CDN-PSMNet** trained with MM ground truths converges much faster. We attribute this to the observations in [2]: a neural network tends to learn simple and *clean* patterns first. We note that, for boundary pixels whose disparities are inherently multi-modal, uni-modal ground truths are indeed *noisy* labels. A network thus tends to ignore these pixels in the early epochs. In contrast, MM ground truths provide *clean* supervisions for these boundary pixels; the network thus can learn the patterns much faster.

Ablation studies. We study different components of our approach in Table 5: methods without W_1 loss use the regression loss for optimization (cf. Equation 2). We see that, the offset sub-network alone can hardly improve the performance. Using W_1 distance alone reduces 1PE and 3PE errors,

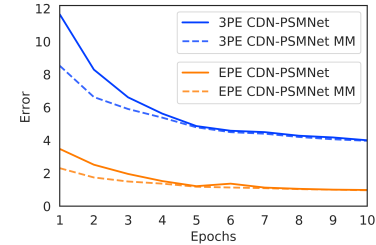


Figure 4: **MM training.** We show the EPE and 3PE disparity errors on Scene Flow test set using **CDN-PSMNet**, w/ or w/o MM training. MM training leads to faster convergence.

Table 5: **Ablation study.** We report Scene Flow disparity error for **CDN-PSMNet**. Methods without W_1 loss use the baseline *mean* regression.

Offsets	W_1 Loss	EPE	1PE	3PE
✓		1.09	12.1	4.56
	✓	1.04	12.0	4.55
✓	✓	1.20	10.5	4.21
✓	✓	0.98	9.1	3.99

8

but not EPE, suggesting that it cannot produce sub-pixel disparity estimates. Only combining the offset sub-network and the W_1 loss produces consistent improvement over all three metrics.

Disparity on boundaries. Table 6 shows the results: we obtain pixels on object boundaries using the Canny Edge Detector. **CDN-PSMNET** reduces the error significantly.

Qualitative Results. We see in Figure 5, that our approach is able to estimate disparity accurately, especially along the object boundaries. Specifically, **CDN-GANET Deep** maintains the straight bar shape (on the right), while **GANET Deep** blends it with the background sky due to the mean estimates.

5 Conclusion

In this paper we have introduced a new output representation, model architecture and loss function for depth/disparity estimation that can faithfully produce real-valued estimates of depth/disparity. We have shown that results not just in more accurate depth estimates, but also significant improvement in downstream tasks like object detection. Finally, because we explicitly output and optimize a distribution over depths, our approach can naturally take into account *uncertainty and multimodality* in the ground truth. More generally, our results suggest that removing suboptimalities in how we represent and optimize 3D information can have a large impact on a multitude of vision tasks.

Acknowledgments

This research is supported by grants from the National Science Foundation NSF (III-1618134, III-1526012, IIS-1149882, IIS-1724282, and TRIPODS-1740822, OAC-1934714), the Office of Naval Research DOD (N00014-17-1-2175), the Bill and Melinda Gates Foundation, and the Cornell Center for Materials Research with funding from the NSF MRSEC program (DMR-1719875). We are thankful for generous support by Zillow, SAP America Inc, AWS Cloud Credits for Research, Ohio Supercomputer Center, and Facebook.

References

- [1] Waymo open dataset: An autonomous driving dataset, 2019. 3
- [2] Devansh Arpit, Stanisław Jastrzębski, Nicolas Ballas, David Krueger, Emmanuel Bengio, Maxinder S Kanwal, Tegan Maharaj, Asja Fischer, Aaron Courville, Yoshua Bengio, et al. A closer look at memorization in deep networks. In *ICML*, pages 233–242, 2017. 8
- [3] Marc G Bellemare, Will Dabney, and Rémi Munos. A distributional perspective on reinforcement learning. In *ICML*, 2017. 6
- [4] Holger Caesar, Varun Bankiti, Alex H. Lang, Sourabh Vora, Venice Erin Liang, Qiang Xu, Anush Krishnan, Yu Pan, Giancarlo Baldan, and Oscar Beijbom. nuscenes: A multimodal dataset for autonomous driving. *arXiv preprint arXiv:1903.11027*, 2019. 3
- [5] Jia-Ren Chang and Yong-Sheng Chen. Pyramid stereo matching network. In *CVPR*, 2018. 1, 2, 3, 7
- [6] Ming-Fang Chang, John W Lambert, Patsorn Sangkloy, Jagjeet Singh, Slawomir Bak, Andrew Hartnett, De Wang, Peter Carr, Simon Lucey, Deva Ramanan, and James Hays. Argoverse: 3d tracking and forecasting with rich maps. In *CVPR*, 2019. 3
- [7] Xiaozhi Chen, Kaustav Kundu, Yukun Zhu, Andrew G Berneshawi, Huimin Ma, Sanja Fidler, and Raquel Urtasun. 3d object proposals for accurate object class detection. In *NIPS*, 2015. 6

Table 6: **Ambiguous regions.** We report the disparity error on Scene Flow.

Method	EPE	1PE	3PE
PSMNet	3.10	20.1	11.33
CDN-PSMNet	2.10	15.3	8.92

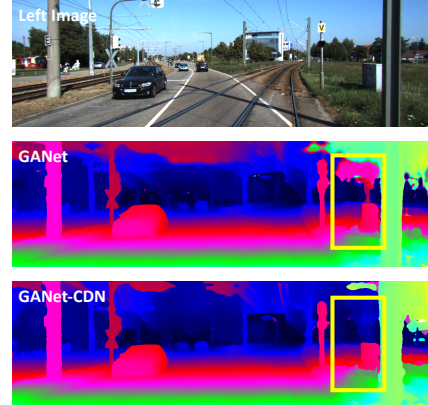


Figure 5: **Qualitative results.** The top, middle, and bottom images are the left image, the result of **GANET Deep**, and the result of **CDN-GANET Deep**.

[8] Xiaozhi Chen, Huimin Ma, Ji Wan, Bo Li, and Tian Xia. Multi-view 3d object detection network for autonomous driving. In *CVPR*, 2017. 6

[9] Yilun Chen, Shu Liu, Xiaoyong Shen, and Jiaya Jia. Dsgn: Deep stereo geometry network for 3d object detection. In *CVPR*, 2020. 1, 3, 6, 7

[10] Andreas Geiger, Philip Lenz, and Raquel Urtasun. Are we ready for autonomous driving? the kitti vision benchmark suite. In *CVPR*, 2012. 2, 3, 6

[11] Andreas Geiger, Philip Lenz, Christoph Stiller, and Raquel Urtasun. Vision meets robotics: The kitti dataset. *The International Journal of Robotics Research*, 32(11):1231–1237, 2013. 3, 6

[12] Xiaoyang Guo, Kai Yang, Wukui Yang, Xiaogang Wang, and Hongsheng Li. Group-wise correlation stereo network. In *CVPR*, 2019. 7

[13] Alex Kendall, Hayk Martirosyan, Saumitro Dasgupta, Peter Henry, Ryan Kennedy, Abraham Bachrach, and Adam Bry. End-to-end learning of geometry and context for deep stereo regression. In *ICCV*, 2017. 1, 2, 3, 7

[14] R. Kesten, M. Usman, J. Houston, T. Pandya, K. Nadhamuni, A. Ferreira, M. Yuan, B. Low, A. Jain, P. Ondruska, S. Omari, S. Shah, A. Kulkarni, A. Kazakova, C. Tao, L. Platinsky, W. Jiang, and V. Shet. Lyft level 5 av dataset 2019. url`https://level5.lyft.com/dataset/`, 2019. 3

[15] Hendrik Königshof, Niels Ole Salscheider, and Christoph Stiller. Realtime 3d object detection for automated driving using stereo vision and semantic information. In *2019 IEEE Intelligent Transportation Systems Conference (ITSC)*, 2019. 3

[16] Jason Ku, Melissa Mozifian, Jungwook Lee, Ali Harakeh, and Steven Waslander. Joint 3d proposal generation and object detection from view aggregation. In *IROS*, 2018. 3

[17] Alex H Lang, Sourabh Vora, Holger Caesar, Lubing Zhou, Jiong Yang, and Oscar Beijbom. Pointpillars: Fast encoders for object detection from point clouds. In *CVPR*, 2019. 3

[18] Buyu Li, Wanli Ouyang, Lu Sheng, Xingyu Zeng, and Xiaogang Wang. Gs3d: An efficient 3d object detection framework for autonomous driving. In *CVPR*, 2019. 3

[19] Peiliang Li, Tong Qin, et al. Stereo vision-based semantic 3d object and ego-motion tracking for autonomous driving. In *ECCV*, 2018. 4

[20] Peiliang Li, Xiaozhi Chen, and Shaojie Shen. Stereo r-cnn based 3d object detection for autonomous driving. In *CVPR*, 2019. 1, 3, 4, 8

[21] Tsung-Yi Lin, Priya Goyal, Ross Girshick, Kaiming He, and Piotr Dollár. Focal loss for dense object detection. In *ICCV*, 2017. 2, 5, 14

[22] Miaomiao Liu, Xuming He, and Mathieu Salzmann. Geometry-aware deep network for single-image novel view synthesis. In *CVPR*, 2018. 1

[23] Wei Liu, Dragomir Anguelov, Dumitru Erhan, Christian Szegedy, Scott Reed, Cheng-Yang Fu, and Alexander C Berg. Ssd: Single shot multibox detector. In *ECCV*, 2016. 2, 5, 14

[24] Xiaofeng Liu, Yang Zou, Tong Che, Peng Ding, Ping Jia, Jane You, and BVK Kumar. Conservative wasserstein training for pose estimation. In *ICCV*, 2019. 6

[25] Nikolaus Mayer, Eddy Ilg, Philip Hausser, Philipp Fischer, Daniel Cremers, Alexey Dosovitskiy, and Thomas Brox. A large dataset to train convolutional networks for disparity, optical flow, and scene flow estimation. In *CVPR*, 2016. 1, 2, 6

[26] Moritz Menze and Andreas Geiger. Object scene flow for autonomous vehicles. In *CVPR*, 2015. 6

[27] Victor M Panaretos and Yoav Zemel. An invitation to statistics in wasserstein space, 2020. 5

[28] George Papandreou, Tyler Zhu, Nori Kanazawa, Alexander Toshev, Jonathan Tompson, Chris Bregler, and Kevin Murphy. Towards accurate multi-person pose estimation in the wild. In *CVPR*, 2017. 1, 2, 5, 14

[29] Alex D Pon, Jason Ku, Chengyao Li, and Steven L Waslander. Object-centric stereo matching for 3d object detection. In *ICRA*, 2020. 3, 8

[30] Charles R Qi, Wei Liu, Chenxia Wu, Hao Su, and Leonidas J Guibas. Frustum pointnets for 3d object detection from rgb-d data. In *CVPR*, 2018. 3

[31] Rui Qian, Divyansh Garg, Yan Wang, Yurong You, Serge Belongie, Bharath Hariharan, Mark Campbell, Kilian Q Weinberger, and Wei-Lun Chao. End-to-end pseudo-lidar for image-based 3d object detection. In *CVPR*, 2020. 1, 3, 4

[32] Aaditya Ramdas, Nicolás García Trillo, and Marco Cuturi. On wasserstein two-sample testing and related families of nonparametric tests. *Entropy*, 19(2):47, 2017. 5

[33] Joseph Redmon, Santosh Divvala, Ross Girshick, and Ali Farhadi. You only look once: Unified, real-time object detection. In *CVPR*, 2016. 2, 5, 14

[34] Daniel Scharstein and Richard Szeliski. High-accuracy stereo depth maps using structured light. In *CVPR*, 2003. 1

[35] Shaoshuai Shi, Xiaogang Wang, and Hongsheng Li. Pointrcnn: 3d object proposal generation and detection from point cloud. In *CVPR*, 2019. 3, 7

[36] Jiaming Sun, Linghao Chen, Yiming Xie, Siyu Zhang, Qinhong Jiang, Xiaowei Zhou, and Hujun Bao. Disp r-cnn: Stereo 3d object detection via shape prior guided instance disparity estimation. In *CVPR*, 2020. 8

[37] Matthew Thorpe. Introduction to optimal transport. 6

[38] Cédric Villani. *Optimal transport: old and new*, volume 338. Springer Science & Business Media, 2008. 2

[39] Yan Wang, Wei-Lun Chao, Divyansh Garg, Bharath Hariharan, Mark Campbell, and Kilian Q. Weinberger. Pseudo-lidar from visual depth estimation: Bridging the gap in 3d object detection for autonomous driving. In *CVPR*, 2019. 1, 3, 6

[40] Yan Wang, Zihang Lai, Gao Huang, Brian H Wang, Laurens van der Maaten, Mark Campbell, and Kilian Q Weinberger. Anytime stereo image depth estimation on mobile devices. In *ICRA*, 2019. 1, 3

[41] Larry Wasserman. Lecture notes in statistical methods for machine learning. 5

[42] Bin Xu and Zhenzhong Chen. Multi-level fusion based 3d object detection from monocular images. In *CVPR*, 2018. 3

[43] Danfei Xu, Dragomir Anguelov, and Ashesh Jain. Pointfusion: Deep sensor fusion for 3d bounding box estimation. In *CVPR*, 2018. 6

[44] Koichiro Yamaguchi, David McAllester, and Raquel Urtasun. Efficient joint segmentation, occlusion labeling, stereo and flow estimation. In *ECCV*, 2014. 2

[45] Bin Yang, Wenjie Luo, and Raquel Urtasun. Pixor: Real-time 3d object detection from point clouds. In *CVPR*, 2018. 3

[46] Gengshan Yang and Deva Ramanan. Upgrading optical flow to 3d scene flow through optical expansion. 2020. 7

[47] Guorun Yang, Hengshuang Zhao, Jianping Shi, Zhidong Deng, and Jiaya Jia. SegStereo: Exploiting semantic information for disparity estimation. In *ECCV*, 2018. 7

[48] Zhichao Yin, Trevor Darrell, and Fisher Yu. Hierarchical discrete distribution decomposition for match density estimation. In *CVPR*, 2019. 7

[49] Yurong You, Yan Wang, Wei-Lun Chao, Divyansh Garg, Geoff Pleiss, Bharath Hariharan, Mark Campbell, and Kilian Q Weinberger. Pseudo-lidar++: Accurate depth for 3d object detection in autonomous driving. In *ICLR*, 2020. 1, 2, 3, 6, 7, 14

- [50] Ye Yu and William AP Smith. Depth estimation meets inverse rendering for single image novel view synthesis. In *European Conference on Visual Media Production*, 2019. 1
- [51] X. Ye X. Tan W. Yang S. Wen E. Ding A. Meng L. Huang Z. Xu, W. Zhang. Zoomnet: Part-aware adaptive zooming neural network for 3d object detection. In *AAAI*, 2020. 3
- [52] Jure Zbontar and Yann LeCun. Stereo matching by training a convolutional neural network to compare image patches. *Journal of Machine Learning Research*, 17:1–32, 2016. 7
- [53] Feihu Zhang, Victor Prisacariu, Ruigang Yang, and Philip HS Torr. Ga-net: Guided aggregation net for end-to-end stereo matching. In *CVPR*, 2019. 1, 2, 3, 7
- [54] Youmin Zhang, Yimin Chen, Xiao Bai, Jun Zhou, Kun Yu, Zhiwei Li, and Kuiyuan Yang. Adaptive unimodal cost volume filtering for deep stereo matching. In *AAAI*, 2020. 3, 7
- [55] Xingyi Zhou, Dequan Wang, and Philipp Krähenbühl. Objects as points. *arXiv preprint arXiv:1904.07850*, 2019. 14

Supplementary Material

We provide in this material the contents omitted in the main paper:

- **Appendix A:** additional implementation details (cf. subsection 3.2 and subsection 4.2 of the main paper).
- **Appendix B:** additional experimental results and analysis (cf. subsection 4.2 and subsection 4.3 of the main paper).

A Implementation Details

A.1 Learning with multi-modal ground-truths

For multi-modal ground-truths, we cannot use [Equation 9](#) of the main paper for optimization. Instead, we apply the loss in [Equation 13](#), for W_1 distance. This loss essentially computes the difference of areas between the CDFs of the two distributions. For mixtures of Dirac delta functions, it can be efficiently implemented by computing the accumulated difference between CDF histograms. It takes $\mathcal{O}(B \log B)$ for each pixel using sorting, where B is the total number of supports of both distributions. Our implementation is adapted from `scipy.stats.wasserstein_distance` and we modify it to be compatible with Pytorch tensors and use CUDA to parallelize the computation over all the pixels.

A.2 The offset sub-network

For our experiments, we add a Conv3D-Relu-Conv3D block to the 4D cost volume (before the last fully-connected or convolutional block of $S_{\text{disp}}(u, v, d)$) to form the offset sub-network $b(u, v, d)$. We predict a single offset $b(u, v, d) \in [0, s]$ for each grid disparity value d , where s is the bin (grid) size. We achieve this by clipping.

A.3 Learning with the (approximated) KL divergence

The *Kullback–Leibler* (KL) divergence

$$KL(\mu||\nu) = \mathbb{E}_\mu \log(\mu|\nu) \quad (14)$$

between two distributions μ and ν requires them to have the same supports: i.e., $\mu(d') = 0$ if $\nu(d') = 0$, for $KL(\mu||\nu)$ to be finite.

For our case, $\mu = \delta(d' - d^*)$ and $\nu = \sum_{d \in \mathcal{D}} p(d|u, v) \delta(d' - (d + b(u, v, d)))$. These two measures may have different supports. To make the KL divergence applicable, we can smooth ν to form a mixture of Laplace or Gaussian distributions.

For example, smoothing ν with a Laplace distribution, $\text{Laplace}(0, \tau) = \frac{1}{2\tau} \exp\left(-\frac{|d'|}{\tau}\right)$, we get

$$\nu_{\text{Lap}}(d') = \sum_{d \in \mathcal{D}} p(d|u, v) \frac{1}{2\tau} \exp\left(-\frac{|d' - (d + b(u, v, d))|}{\tau}\right). \quad (15)$$

With ν_{Lap} , the KL divergence reduces to the following loss

$$\ell(\mu, \nu_{\text{Lap}}) = -\log \sum_{d \in \mathcal{D}} p(d|u, v) \frac{1}{2\tau} \exp\left(-\frac{|d^* - (d + b(u, v, d))|}{\tau}\right) \quad (16)$$

$$\approx -\log p(\bar{d}|u, v) + \frac{1}{\tau} |d^* - (\bar{d} + b(u, v, \bar{d}))|, \quad (17)$$

where $\bar{d} = s \lfloor \frac{d^*}{s} \rfloor \in \mathcal{D}$ is the grid disparity value of the bin the true disparity d^* belongs to.

Similarly, smoothing ν with a Gaussian distribution $\mathcal{N}(0, \sigma^2)$, we get

$$\nu_{\text{Gau}}(d') = \sum_{d \in \mathcal{D}} p(d|u, v) \frac{1}{\sigma\sqrt{2\pi}} \exp\left(-\frac{\|d' - (d + b(u, v, d))\|_2^2}{2\sigma^2}\right). \quad (18)$$

Table 7: **Comparison of different divergences (distances).** We report the RMSE and the ABSR error for depth estimation on Scene Flow. The best result of each column is in bold font.

Method	Divergence	RMSE (m)	ABSR
SDN	-	2.05	0.04
CDN-SDN	KL	2.57	0.04
CDN-SDN	W_1	1.81	0.03
CDN-SDN	W_2^2	1.91	0.05

Table 8: **Comparison of bin sizes.** We report the disparity error on Scene Flow using **CDN-PSMNET** model.

Bin size	EPE	1PE	3PE
1	1.22	13.9	4.33
2	0.98	9.1	3.99
4	1.52	26.1	4.17

With ν_{Gau} , the KL divergence reduces to the following loss

$$\ell(\mu, \nu_{\text{Gau}}) = -\log \sum_{d \in \mathcal{D}} p(d|u, v) \frac{1}{\sigma\sqrt{2\pi}} \exp\left(-\frac{\|d^* - (d + b(u, v, d))\|_2^2}{2\sigma^2}\right) \quad (19)$$

$$\approx -\log p(\bar{d}|u, v) + \frac{1}{2\sigma^2} \|d^* - (\bar{d} + b(u, v, \bar{d}))\|_2^2, \quad (20)$$

where $\bar{d} = s \lfloor \frac{d^*}{s} \rfloor \in \mathcal{D}$ is the grid disparity value of the bin the true disparity d^* belongs to.

These formulations reduce to the conventional classification loss plus offset regression loss, commonly used for keypoint estimation [28, 55] and one-stage 2D object detection [21, 23, 33, 55].

B Additional Results and Analysis

B.1 Ablation studies on different divergences

We show the ablation study on using different divergences between distributions in Table 7. For the KL divergence (subsection A.3), we use Laplace smoothing with $b = 1$ (Equation 17). Our results show that the Wasserstein distance is a better choice than the KL divergence for comparing the predicted and the ground-truth disparity (or depth) distributions. We also see that W_2^2 distance performs worse than W_1 . We attribute this to outliers (i.e., noisy disparity labels) in a dataset.

B.2 Effect of bin sizes

We show the effect of bin sizes on uniform grids with disparities in the range of $[0, 191]$ for stereo disparity estimation in Table 8. For a bin size $s = 1$, predicting the correct bin becomes harder. For a bin size $s = 4$, predicting the correct bin is easier, whereas predicting the correct offset becomes harder.

B.3 Point cloud visualization

Figure 6 shows the BEV point cloud visualization. We show the 3D points generated by SDN and **CDN-SDN** as well as the ground-truth LiDAR points and car/pedestrian boxes. We see that, **CDN-SDN** generates sharper points than SDN. Specifically for pixels on the foreground objects, SDN usually predict the depths beyond the boxes due to the *mean* estimates from multi-modal distributions on the boundary pixels, whereas **CDN-SDN** significantly alleviates the problem. We also see some failure cases of **CDN-SDN**: on the right image, **CDN-SDN** has a larger error on the background compared to SDN.

B.4 Depth estimation

Besides the Scene Flow dataset, we show the depth estimation error on KITTI Val: the 3,769 validation images for 3D object detection. We follow [49] to compute the depth estimation error on

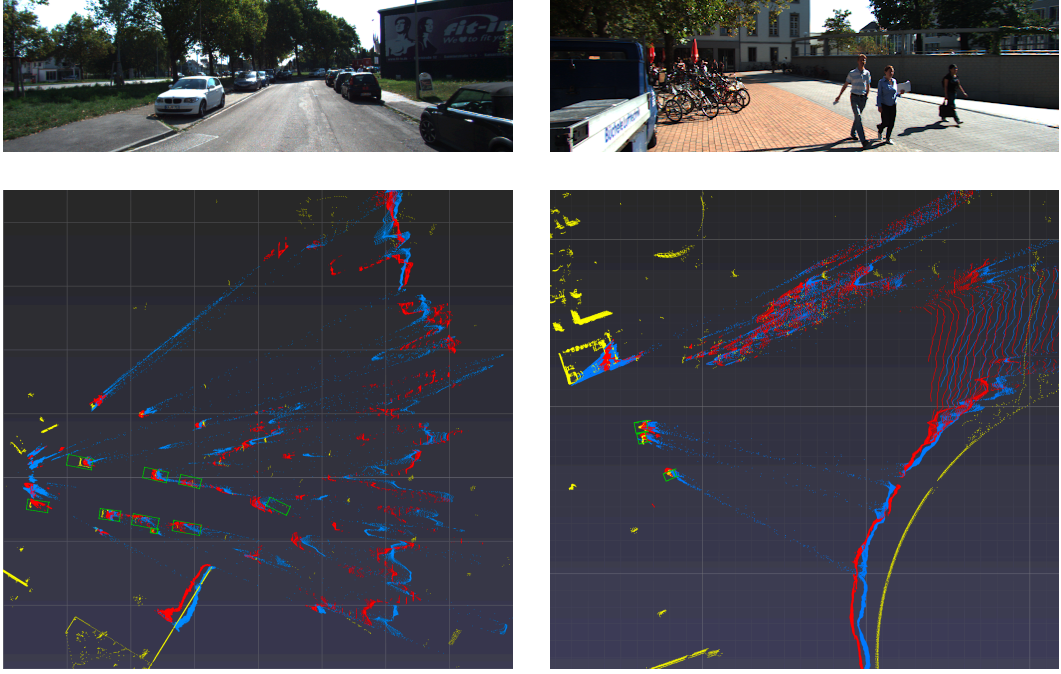


Figure 6: **BEV Point cloud visualization.** The blue points are obtained using SDN. The red points are from our **CDN-SDN** model. The yellow points are from the ground-truth LiDAR. The green boxes are ground-truth car / pedestrian locations. The observer is at the left-hand side of the point cloud looking to the right.

Table 9: **Depth error on KITTI Val.** We compare SDN and **CDN-SDN** models.

Method	Depth errors (m)	
	Mean	Median
SDN	0.589	0.128
CDN-SDN	0.524	0.093

pixels associated with ground-truth LiDAR points. Table 9 and Figure 7 show the results, **CDN-SDN** achieves lower error than SDN, which explains why **CDN-SDN** (and **CDN-DSGN**) can lead to better 3D object detection accuracy.

B.5 3D object detection

We show in Figure 8 the object detection precision-recall curves of DSGN vs. **CDN-DSGN**. **CDN-DSGN** has higher precision (vertical) values than DSGN at different recall (horizontal) values.

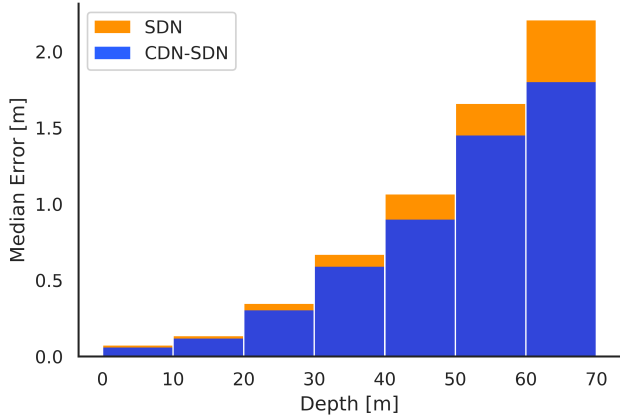


Figure 7: **Depth error on KITTI Val.** We compute the median absolute depth error for different depth ranges on KITTI Val images using SDN and **CDN-SDN**.

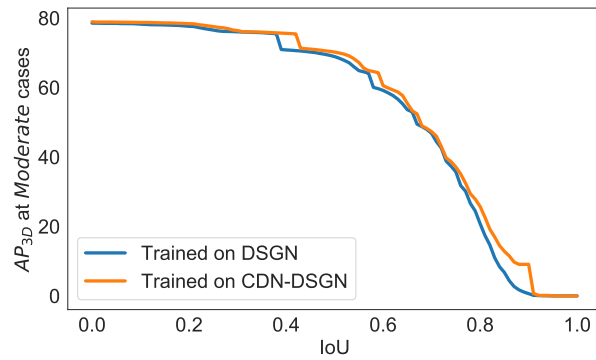


Figure 8: We show the object detection precision-recall curves for AP_{3D} at moderate cases on cars. We compare DSGN (stereo images) and **CDN-DSGN** (stereo images).